IEEE Journal on Exploratory Solid-State Computational Devices and Circuits

Received 10 May 2015; revised 29 May 2015 and 23 July 2015; accepted 9 August 2015. Date of publication 13 August 2015; date of current version 28 October 2015.

Digital Object Identifier 10.1109/JXCDC.2015.2468070

Physical Implementation of Coherently Coupled Oscillator Networks

MATTHEW R. PUFALL[1], WILLIAM H. RIPPARD[1], GYÖRGY CSABA[2], DMITRI E. NIKONOV[3], GEORGE I. BOURIANOFF[4], AND WOLFGANG POROD[2]

[1]National Institute of Standards and Technology, Boulder, CO 80305 USA
[2]Center for Nano Science and Technology, University of Notre Dame, Notre Dame, IN 46556 USA
[3]Intel Corporation, Hillsboro, OR 97006 USA
[4]Intel Corporation, Austin, TX 78746 USA

CORRESPONDING AUTHOR: G. CSABA (gcsaba@nd.edu)

This work was supported by Intel Corporation.

This work has supplementary downloadable material available online at http://ieeexplore.ieee.org, provided by the authors. This includes a PDF file which contains information regarding the modeling of STOs in a circuit environment. This material is 334 KB in size.

ABSTRACT We present a combined experimental and simulation study of the physical implementation of coherently coupled oscillator networks composed of spin-torque oscillators (STOs). Based on published works and on our recent experiments, we review the behavior of individual oscillators and arrays of coupled oscillators. We construct models that are calibrated by experiments, and our simulations demonstrate that an array of coherently coupled STOs exhibits the basic functionality of an associative memory.

INDEX TERMS Associative processing, non-Boolean computing, oscillator synchronization, spin-torque oscillators (STOs).

I. INTRODUCTION

THIS paper is the third in the series of papers in this special section. As discussed in [1] and [2], the tendency of coupled nonlinear oscillators to phase lock can be exploited to implement associative clusters. These implementations map the physics of phase locking to the associative process. In this paper, we discuss such associative memory architectures implemented in coupled arrays of spin-torque oscillators (STOs). STOs are promising candidates for the oscillators that comprise these architectures, due to their small sizes and multiple nonlinearities. STOs respond nonlinearly to ac currents, fields, and spin waves (the fundamental excitations in a ferromagnetic medium), which provide multiple methods for coupling oscillators together.

In this paper, we first describe the structure and magnetization dynamics of individual, uncoupled STOs. Then, we discuss the experimental evidence for frequency locking in STOs coupled by spin waves mediated by a common ferromagnetic layer. Next, we describe our modeling approach, first for individual and then for coupled STOs. Based on these models, we then simulate the behavior of an associative cluster, and demonstrate its functionality in the associative memory architecture.

The spin transfer effect is the transfer of angular momentum from a spin-polarized current to a local magnetic moment, and is a means to manipulate nanoscale magnetic devices and induce magnetization dynamics without the need for applied fields. The spin transfer effect was first predicted by Slonczewski [3] and Berger [4], and subsequently observed by several groups in a variety of device geometries [5]–[8]. The torque induced by a spin-polarized current traversing a magnetic material can counteract the local damping torque, thus causing an instability, and motion of the magnetization. Depending on the energy landscape of the magnetic system, this motion results in magnetization switching, as used in the spin-torque magnetic RAM, or in coherent magnetic precession that is the basis of STOs. STOs are particularly promising for applications that require compact arrays of oscillators, because the spin transfer effect becomes more efficient with decreasing size, and because of their high operating frequencies (1–50 GHz) and nonlinear responses to ac signals.

The dynamics of the magnetization distribution is governed by the local magnetic environment, which produces a net effective field around which the magnetization precesses. The net effective field is the sum of externally applied fields, anisotropy fields, exchange fields, electron-current-induced fields, spin-transfer-induced effective fields, and the demagnetizing fields produced by the magnetization itself. As has been described previously [5], [6], even in the

single-domain approximation, STOs are nonlinear systems. The nonlinearities of this system and the sensitivity to the details of the local magnetic environment give rise to complex dynamics, and also allow STOs to phase lock to external signals and to each other. A detailed discussion of STO dynamics can be found in [7]. What follows is a basic discussion of dynamics necessary to describe phase-locking processes in STOs. Several aspects of STO dynamics have been studied extensively in the recent years—we review the physical processes that may be utilized to produce the arrays of phase-locked STOs for information processing.

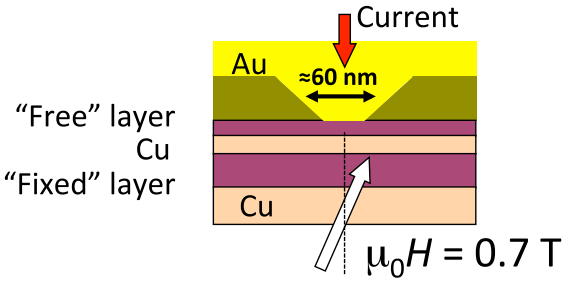

FIGURE 1. Schematic of a typical STO. The magnetic layers extend to form an 8 μm x 20 μm mesa, while the spin torque is exerted only in the vicinity of the nanocontact region where current flows. Changing the applied field angle θ or magnitude alters the dynamics excited by spin torque.

II. STO EXPERIMENTS

A typical nanocontact STO structure is shown in Fig. 1, and consists of a <100 nm diameter electrical contact made to a ferromagnet/nonmagnet/ferromagnet spin-valve multilayer structure. One ferromagnetic layer (FM1), called the free layer, is chosen to have a lower total moment, either via reduced thickness and/or magnetization M, than the second ferromagnetic layer (FM2), so that FM1 is more susceptible to the effects of spin torque than is FM2. Spins entering a ferromagnetic layer are not transmitted equivalently: spins parallel to the local moment are preferentially transmitted, while spins antiparallel are preferentially reflected. Consequently, any spin component transverse to the magnetization is absorbed by the ferromagnet, exerting a torque that in turn can result in motion of the magnetization.

Fig. 2 shows power spectra for several dc currents from an STO consisting of a 60-nm diameter nanocontact, 4-nm $Ni_{80}Fe_{20}$ free layer, 4-nm Cu spacer layer, and 10-nm CoFe fixed layer, for an applied field of $\mu_0 H = 0.7$ T applied at 10° from the surface normal. The frequency increases or blue shifts with increasing current because as the spin torque increases the cone angle of precession, the magnitude of the out-of-plane demagnetization field decreases, thus increasing the net effective field and hence the operating frequency. In contrast, for the in-plane applied fields, the net internal effective magnetic fields decrease with increasing precessional cone angle, and the precession frequency red shifts with current. This demonstrates how the internal

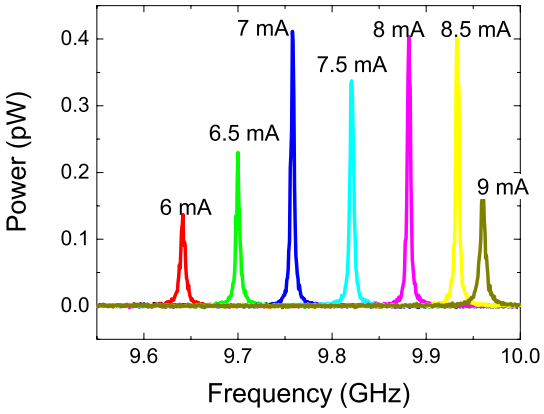

FIGURE 2. Power spectral density versus frequency for several currents for NiFe 4-nm/Cu 4-nm/CoFe 10-nm nanocontact. $\mu_0 H = 0.7$ T and $\Theta_H = 10°$, from sample geometry given in Fig. 1. Resolution bandwidth is 1 MHz. Frequency shift and amplitude change with current demonstrate two nonlinearities of STO dynamics.

effective magnetic fields largely determine the precession frequency of STOs [8]. For typical magnetic materials and laboratory applied fields, frequencies of nanocontact STOs are in the range of 1–50 GHz, and this scale set by the gyromagnetic ratio $\approx$ 28 GHz/T for electrons in ferromagnets. The amount that the oscillator tunes with current depends on the variation of the net effective field with a precession cone angle as described above, but also may depend on the details of the excitation mode not captured by the single-domain approximation. The specific details are not yet well understood [9]. Micromagnetic modeling is presently being used to understand how these local excitations in continuous layers, which may experience additional exchange fields due to magnetization gradients, differ from those of patterned materials. This comparison is discussed in more detail in Section IV. The linewidth of nanocontact STOs is in the range of 1–100 MHz and largely results from thermal fluctuations in the system. This is narrower than that of oscillators based on nanopillar structures in which the magnetic multilayers are patterned into a columnar structure. This difference is likely due to the larger effective volume of the nanocontact structure, and the lack of patterned edges that may have differing magnetic properties. Beyond thermal fluctuations, additional 1/frequency noise processes also contribute to the oscillator frequency noise spectrum [10], via processes whose microscopic origins are still being explored.

III. PHASE LOCKING

A. INJECTION LOCKING

STOs frequency pulls and phase locks to impressed ac signals due to the combined nonlinearities of the large-angle magnetization motion in STOs and the interaction between the spin-polarized current and the STO's magnetic moment [11], [12]. As shown in Fig. 3 (taken from [11]), upon injecting an ac signal into an STO, the oscillator frequency pulls toward

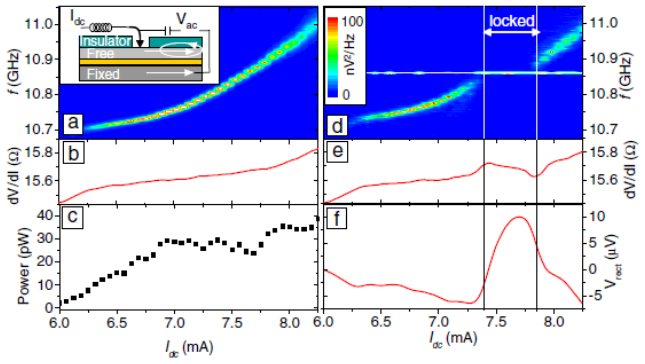

FIGURE 3. **Injection locking of an STO. (a) Free-running oscillator output. Inset: device schematic. (b) *dV*/*dI* of free running device. (c) Output power of device versus I_{dc}. (d) Device output with $f = 10.86$ GHz, amplitude = 410 μA (rms) injected signal. (e) and (f) *dV*/*dI* and rectification voltage for injected-locked device. Figure from [11].**

the injected signal, and jumps to the injected signal's frequency when the frequencies are sufficiently close.

An analysis of the spectral output and the time-domain measurements show that the STO has, on average, a fixed phase relationship to the injected signal, and largely takes on the noise characteristics of the injected signal. As shown in Fig. 3(a), the frequency of the free-running oscillator increases as the current is increased through the contact. In the phase-locked case [Fig. 3(d)], the STO shows the behavior typical of injection-locked oscillators, with the frequency remaining fixed at the injection frequency, while the phase of the STO relative to the drive signal shifts by ~180° over the locking range (see Fig. 4). A few theories approximately describe (with varying degrees of success) this STO locking behavior and also the manner in which STOs lock to harmonics (see below) [6], [13].

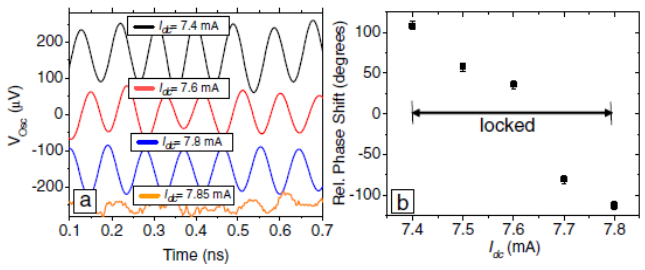

FIGURE 4. **(a) Voltage versus time from an STO for different dc bias currents. Data are taken stroboscopically and averaged on a sampling oscilloscope with 40-GHz bandwidth, so an ac signal from the STO is measured only if the STO has a defined phase relationship to the time reference, which was taken from the injected ac signal. (b) Phase relative to injected signal, versus dc current through device. From [11].**

To function in a practical oscillator-based associative memory, STOs must respond quickly to impressed signals. The previous work has shown that STOs can be modulated by injected ac currents with modulation bandwidths greater than a gigahertz [13]. Recently, STO response time was determined by directly measuring the time to lock an STO to an injected ac current [14]. In this measurement, a pulsed ac current was injected into an STO at $2f$, where f is close to the STO free-running oscillation frequency (in this case 10.45 GHz). After bandpass filtering with a microwave filter centered around f, the device response was measured and averaged with a real-time oscilloscope triggered phase synchronously with the pulsed RF. The pulse length was 100 ns, and the repetition time was 1000 ns, much longer than the measured STO decoherence time (≈50 ns). As shown in Fig. 5, no oscillatory signal is visible above the noise before the pulse, as expected for an averaged measurement of a phase incoherent signal. After the pulse arrives, the STO signal grows, reaching a constant value after a period that depends on the injected signal amplitude.

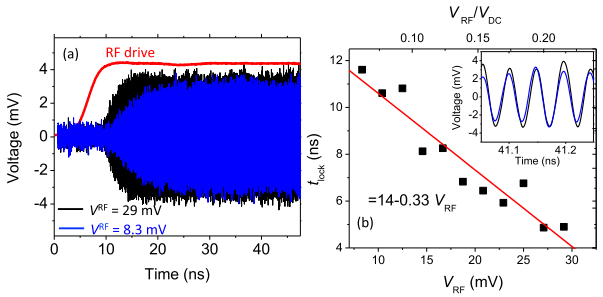

FIGURE 5. **Injection locking (a) STO voltage versus time. Traces are averages of 4096 real-time traces. Red solid line: timing and amplitude envelope of RF pulse. (b) Time between pulse and STO 90% points versus RF voltage amplitude. Inset: teal-time traces showing phase for two RF drive amplitudes, showing that phase is stable relative to drive amplitude. Device and measurement setup similar to that in Figs. 3 and 4. From [14].**

These results are relevant to phase locking in STO arrays in several ways. First, devices can be phase locked to RF currents at harmonics of the device response (as has also been observed for field locking as described in Section III-B) [12]. This implies that the magnetization orbit is not perfectly circular, having some component at the second harmonic that couples to the RF signal, or that the ac spin torque is not constant over the orbit. Second, phase locking to a signal at twice the free-running oscillator frequency occurs on time scales on the order of 5–10 ns for these drive amplitudes, or roughly 50–100 device oscillations. Finally, if phase initialization is required for array operation, the time between initialization and operation must be much less than the 50-ns decoherence time. These characteristic times are a consequence of the nanoscale device size, on which thermal fluctuations have a significant impact [10], [15], and the intrinsic damping of magnetic materials.

B. FIELD LOCKING

For STOs to be arrayed in a viable technology, the nonlinearities that couple the STOs together must be better understood, as must mechanisms underlying the variations in frequency

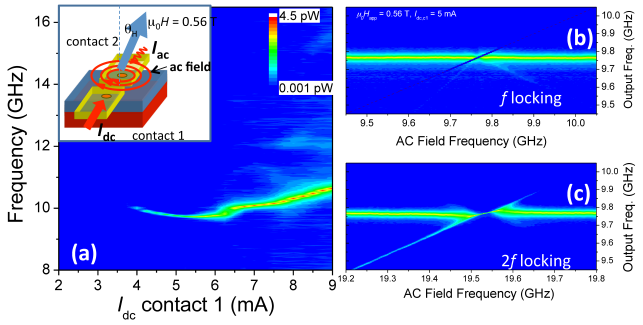

FIGURE 6. Field locking to harmonics. (a) Free running oscillations for $\mu_0 H = 0.56$ T, $\theta H = 10°$. Inset: device and measurement schematic. (b) Spectral output versus injected frequency near f_{osc} (≈9.76 GHz) for $I_{dc} = 5$ mA. (c) Spectral output versus injected frequency near $2f_{osc}$ for $I_{dc} = 5$ mA.

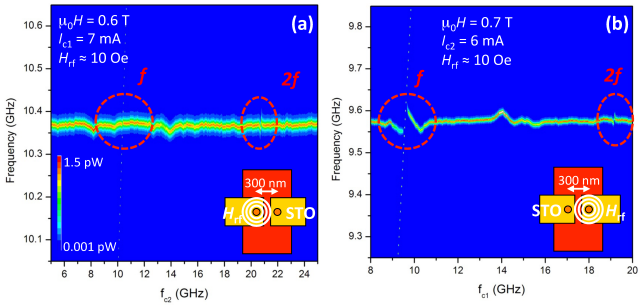

FIGURE 7. Device-to-device phase locking variations for two nanocontacts made to the same NiFe/Cu/CoFe magnetic mesa. (a) Right contact (1) as STO, left contact as RF field source. (b) Right contact as RF field source, left contact (2) as STO. Dashed circles: locations of f, $2f$ for each case.

from device to device. Measurement of locking to harmonics is a way to parameterize the nonlinearity of the system for the development of efficient models [12], [13], and to quantify device-to-device variations. For example, Fig. 6 shows phase locking to ac fields as a function of frequency for frequencies around both f_{osc} and $2f_{osc}$, in which f_{osc} is the oscillator frequency. In this measurement, two-independent nanocontacts spaced 300 nm apart are made to the same NiFe (5 nm)/Cu (4 nm)/CoFe (10 nm) magnetic mesa. One contact is dc current-biased as an STO, while the other is used as an ac field source by injecting an ac current into it, producing a circumferential ac magnetic field [see Fig. 6(a) (inset)]. This ac current will produce some disturbance of the magnetization at the field-source contact, producing spin waves that could radiate to the second contact. However, the amplitude of such spin waves is estimated to be too small to significantly contribute to the locking dynamics, because the spin waves are alternately damped every half cycle of the current.

Fig. 6(a) shows the free-running output from one STO as a function of current. Fig. 6(b) and (c) shows the output for $I = 5$ mA (producing an f_{osc} of ≈9.76 GHz) as a function of frequency of the RF signal injected into the second contact. The amplitude of the RF current is chosen to produce roughly a 1-mT (10 Oe) field at the active STO. The STO frequency pulls and phase locks as the frequency of the ac field approaches f_{osc} and $2f_{osc}$. The relative sizes of the locking ranges may be useful as measures of the strengths of an STO's nonlinear response to fields [14], and as a benchmark of compact models of STOs. These models are necessary for simulating large coupled arrays, as described later in this paper. Unlike in [12], locking to fractional harmonics was not observed, perhaps due to the different field geometries, and thus different orbits excited by the dc current in this geometry.

The nonlinear response can also be used to benchmark device-to-device variations. In Fig. 7, we show spectral output from a pair of nanocontacts measured in the manner described for the results in Fig. 6. In this case, we measure one configuration—contact 1 as an STO, and contact 2 as a field source—and we then reverse the roles of the nanocontacts. Despite being similar nanocontacts made to the same magnetic mesa, the two STOs behave differently. The frequencies are substantially different, with contact 1 having a higher frequency despite being measured in a lower field. Also, the frequency pulling and locking for contact 1 is also much weaker than for contact 2, showing little evidence of locking to f. Device-to-device variations in nanocontact STOs are just beginning to be studied in a rigorous way [9], [15], and the impacts of small variations in magnetization or contact structure are not well characterized. However, the above results indicate that such variations may have a substantial impact on the resulting nonlinear device behavior. Accounting for device variations will be critical to the function of larger coupled arrays.

C. LOCKING VIA SPIN WAVES

Phase locking between nanocontact pairs has been shown previously to be largely mediated by spin waves [15]–[17]. Coupling of large arrays of STOs in this fashion is an attractive possibility, as this would make unnecessary an additional wiring layer for coupling. However, with the notable exception of magnetic vortex oscillators [18], the coupling of more than two STOs via spin waves has been largely unexplored. Issues, such as spin-wave propagation anisotropy and frustration, may affect the array locking dynamics. As a rudimentary test of such arrays, we fabricated devices consisting of an array of four 75-nm diameter nanocontacts made to a single magnetic mesa that are electrically connected in parallel by a common top electrode. The magnetic mesa consists of a CoFe/Ni multilayered free layer whose magnetization is compensated by an out-of-plane surface anisotropy, such that $\mu_0 M_{\text{eff}} = \mu_0(H_k - M_s) \approx 0.1$ T out of plane. This induces a large angle between the fixed and free layers, and results in both a larger spin torque and larger giant magnetoresistance readout signal. The stack is a sputtered multilayer with a Ta3/CuN10/Ta3/Cu3/CoFe10/Cu5/CoFe0.3[Ni0.45/CoFe0.3]5/Cu3/Ta3 (thicknesses in nanometer) layer structure. Here, the free layer corresponds to the Ni/CoFe multilayer.

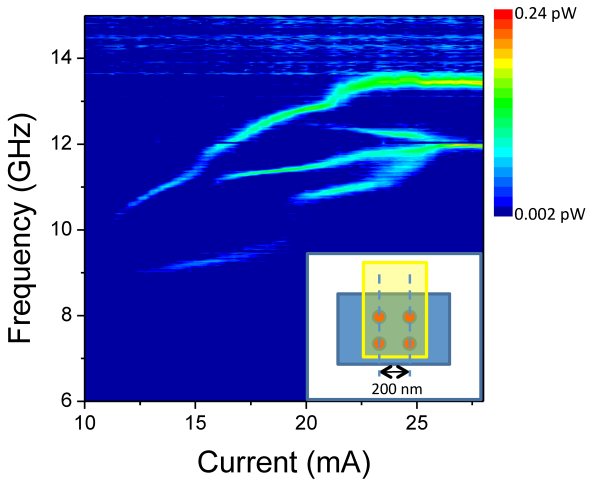

FIGURE 8. **Spectral output versus current for four contact array. Applied field 0.4 T out of plane. Inset: device schematic.**

Because the currents through the individual contacts are not individually controllable, device-to-device variations (such as shown in Fig. 7) may make the frequency differences between some of the contacts too large to allow locking. As shown in Fig. 8, one can see that there is indeed a significant contact-to-contact variation within a four contact array. For example, at 13 mA, only two peaks are visible, while at ≈21 mA four peaks are seen, spread over ≈2.5 GHz. These peaks move toward each other as the current is increased, and three of the four peaks merge into a single, narrow peak by 26 mA. This frequency-pulling behavior, the linewidth narrowing, and the power increase that occurs when the peaks merge are consistent with phase locking. These results indicate that even in this nonideal system, i.e., a system with significant magnetic inhomogeneities that lacks the ability to independently control each nanocontact frequency, phase locking of more than two devices is possible. Further measurements of multicontact arrays with different topologies, independently controllable devices, and more uniform magnetic materials and fabrication techniques are needed to better understand the physics governing larger spin-wave-coupled arrays. The geometry of the STO placement will determine the coupling between STOs, and this severely limits the realizable coupling scenarios [21].

IV. CIRCUIT MODELS AND SIMULATION OF INJECTION LOCKING IN A STAND-ALONE STO

Circuit models are useful to understand the behavior of nanodevices (such as STOs) in a circuit environment. A short overview of our STO circuit models is given in the supplementary material. The simulations below show results from the circuit model of a Permalloy-based STO, with parameters chosen to be similar to the STO of Fig. 3.

We have not attempted to exactly reproduce the experimentally observed behavior of this STO, as it is quite challenging to do without any parameter fitting. For the in-plane magnetized, nanocontact STOs, the oscillation frequency and amplitudes are very sensitive to the model parameters, such as the precise direction of **S**, the contact area, the damping constant, and the Λ and P spin transfer parameters. A relatively small change to any of these parameters may cause a large rotation in the oscillation axis, significantly altering the frequency.

Macrospin model-based simulations are shown in Fig. 9(a). The oscillation threshold and the frequency at the threshold are correctly predicted by this simple model. The simulations clearly show the blueshifting of the oscillation frequency with increasing current—this is caused by the out-of-plane component of **S**, which pushes the oscillation orbit out of plane, increasing the net $\mathbf{H}_{\text{eff}}$ field. The macrospin simulations give a much steeper blueshift of oscillation frequency than the experimental data of Fig. 3.

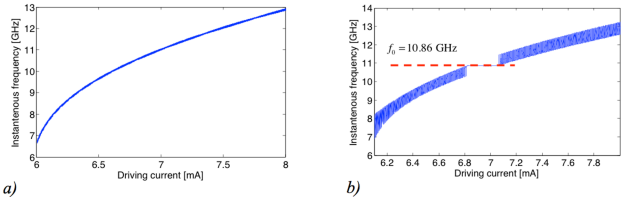

FIGURE 9. **(a) Plot of the calculated frequency versus current relation $f(i)$ of an STO in the macrospin approximation. (b) Plot of frequency versus current for the same STO injection locking to an impressed $f_0 = 10.86$-GHz ac current. The simulated device is similar to the one experimentally studied in Fig. 3.**

Fig. 9(b) shows the effect of a 10.86 GHz ac-injected current with $i = 410\ \mu$A on the modulation on the STO frequency. In agreement with the experiments, this STO frequency is locked to the injected current frequency for a range of currents. The numerically calculated locking range is smaller than the experimentally observed range, which is a consequence of the steeper $f(i)$ relation in the simulation. The numerical simulation also clearly shows that the oscillation linewidth abruptly decreases upon locking, but it is relatively large just before the onset of synchronization and just after the STO decouples from the injected frequency.

We have chosen to show an in-plane STO in the above example, but we remark that it is generally much easier to get good agreement between the experimental and simulated $f(i)$ curves for the out-of-plane magnetized STOs (such as the CoFe/Ni STOs [19]). The out-of-plane anisotropy defines a rotation axis for the magnetization vector eliminating some degree of freedom from the spin dynamics.

V. TIME DEPENDENCE OF LOCKING AND FIELD-LOCKING

Simulations on the circuit model reveal that the details of the injection-locking process are complex and depend strongly on the initial phase relation between the STO and its modulating signal, which at finite temperature will be random. Fig. 10(a) shows the time dependence of the STO frequency as a function of time in response to the abrupt injection

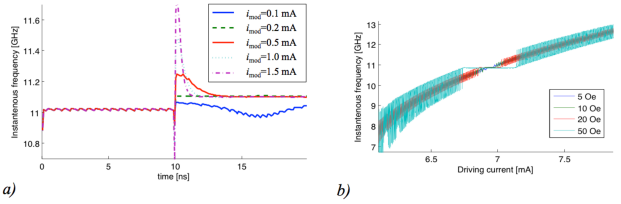

FIGURE 10. (a) Time-dependence of frequency of the STO in response to injection of ac currents with $f_{ac} = 11.1$ GHz of different amplitudes. For most amplitudes, locking occurs in $dt < 5$ ns. (b) STO locking-in response to an oscillating external field, showing behavior similar to that seen in response to an injected current. The instantaneous frequencies are calculated from the time period of the oscillations.

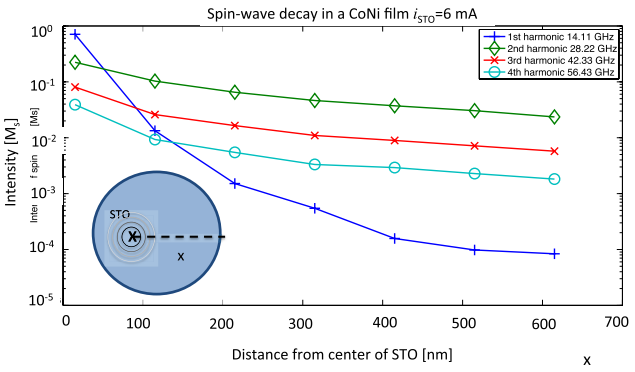

FIGURE 11. Intensity of different harmonics of the spin wave as a function of distance from the STO. The lines are a guide to the eye. The harmonics show more gradual decay with distance than the fundamental frequency.

of an ac current at ($t = 10$ ns) into a free-running dc-biased STO. The instantaneous frequencies are calculated from the time-period of the oscillations. One can see that for $i_{mod} = 0.2$ mA locking occurs instantaneously. For most other cases, the frequency first overshoots and then converges to the locking frequency. Consistent with the experimental results shown earlier in this paper, the locking time is in the few nanoseconds range, and perfect locking occurs in less than 5 ns and fewer than 100 oscillation cycles.

Fig. 10(b) shows the simulation of field-locking in the macrospin model. We complemented the circuit model with a field port that enables the modulation of the external field and simulates a scenario similar to the one described in Section III-B. Modulations on the order of 1 mT result in a robust locking over several hundred microamperes of driving current range.

VI. SPIN-WAVE INTERCONNECTED STOs

As pointed out in Section III-C, a special advantage of nanocontact STOs is that the short-range interconnections between devices can be established magnetically. If multiple STOs are placed on the same magnetic film, then the outward-radiating spin waves of an STO reach nearby STOs and may synchronize their oscillations. This was first demonstrated experimentally in [15], and Section III-B of this paper discusses the evidence of spin-wave coupling between nearby STOs.

Modeling spin-wave propagation requires using a full micromagnetic model and can be done readily using a standard micromagnetic code, such as OOMMF [20]. As an example, Fig. 11 shows the intensity of spin waves in a CoNi film with the out-of-plane anisotropy as a function of distance from the STO. The graphs were calculated by driving the STO with a constant current and Fourier transforming the $\mathbf{M}(t)$ magnetization at 100 nm spaced points away from the center of the oscillator. A strongly driven STO generates a number of harmonics, and this method enables an investigation into the behavior of each frequency component separately.

Note that for a full spin-wave characterization, one needs to determine the phase delay of the spin wave and the time delay associated with the wave (spins wave propagate typically with a $v \sim 1000$ m/s speed). For the sake of simplicity, we focus now only on the spin-wave amplitude.

Fig. 11 shows the decay of spin waves at multiples of the lowest frequency excitation of the STO, as a function of distance from the STO. The decay of such waves will be governed by $1/r$ geometric loss, magnetic damping losses related to Landau–Lifshitz damping, and by the frequency dependence of the magnetic medium, which is set by the spin-wave dispersion relation in the medium. In Fig. 11, one can observe that the lowest frequency mode has the largest amplitude of all modes in the vicinity of the STO. However, because its frequency in this case lies below the ferromagnetic resonance (FMR) frequency of the surrounding medium (i.e., the cutoff frequency), the amplitude diminishes rapidly with distance away from the contact. For the higher harmonics, the decay is much slower and for $r > 100$ nm obeys the $M_{osc} = (M_0 C \exp(-r/\lambda))/r$ expression, where M is the oscillation amplitude at distance r from the STO center, M_0 is the oscillation amplitude at the center of the STO, C is describing an insertion loss that quantifies how efficiently the STO injects spin waves into its immediate surroundings, and λ is a spin-wave decay due to Landau–Lifshitz damping in the film. Expressions similar to (2) were also verified experimentally [23]. The propagation of spin waves above the FMR frequency is characterized by similar λ and C constants.

Equation (2) enables approximate modeling of spin-wave coupling in the framework of the macrospin model. The key to this is to define an effective $\mathbf{H}_{eff}^{osc}$ coupling field between two or more STOs that generates the same M_{osc} amplitude oscillations as the spin waves and include this effective field in the equivalent circuit as a field driving term. For example, consider two STOs, placed 500 nm apart. We assume the spin-wave decay characteristic of Fig. 11, and that the interaction occurs via the second harmonic. In this case, one of the STOs (STO1) creates $\sim 0.05\ M_s$ amplitude spin waves at the position the second STO (STO2). STO2 is subjected to spin wave that a 1 mT (10 Oe) external field would

create—this can be estimated from the hard-axis hysteresis curve of the STO2 free layer. Therefore, the locking behavior can be described by the corresponding 10 Oe curve of Fig. 10. This way spin-wave interaction can be modeled in the same framework as electrically or field-coupled STOs. See [21] for a more rigorous way of deriving a coupling coefficient between STOs.

Clearly, up to at least 500-nm distance, spin-wave coupling provides an efficient mechanism for interconnecting STOs, and it comes for free without requiring any additional circuitry. The coupling strengths between STOs will be determined by the geometry, which restricts what kind of circuit functions can be realized.

VII. ELECTRICAL INTERCONNECTION OF STOs

Electrical coupling provides flexible possibilities to tune interaction strength between STOs. The details of the interconnecting circuit largely depend on the type of magnetoresistive behavior exhibited by the STO. The magnetization oscillations of metallic Giant Magnetoresistance (GMR)-based STOs modulate a resistance of a few ohms by a few percent, while Magnetic Tunnel Junction (MTJ)-based STOs have much larger (kΩ) resistances, and modulations of several tens of percent, potentially producing much larger electric signals.

Active electrical interconnection schemes rely on CMOS circuitry that amplify magnetoresistive signals and reapply them to electrically modulate the STOs [22]. This gives full flexibility of choosing arbitrary coupling schemes, though the substantial additional CMOS circuitry may be needed.

VIII. ASSOCIATIVE CLUSTERS BASED ON STO INTERACTIONS

The understanding of oscillator interactions in an STO network paves the way to using them as building blocks of dynamic computing systems. A number of proposals exist for such computing systems [22], [24]–[26], and we study two particular systems as application examples. In the first one (coupled-oscillator associative memory array (COAMA) [1], [2], [24]), the coupling strength of the STOs is modulated by differences in oscillator frequency. In the second scheme, the coupling is mediated by frequency modulation of the constituent oscillators [25]. A number of papers in this special issue are devoted to the COAMA scheme, and the reader can refer to [1], [2], and [22] for details.

The COAMA scheme uses an oscillator array to create a pattern-matching network operating in the frequency domain. The goal is to determine whether the A and B vectors are sufficiently similar to each other, i.e., whether the distance between them is above or below a certain threshold. The A and B vectors may represent the pixel intensities of an image or an image patch.

We assume that A and B are analog current values, and the input of the oscillator network is the element-wise difference of the vectors, $I = A - B$. The length of the I vector is related to the similarity of A and B.

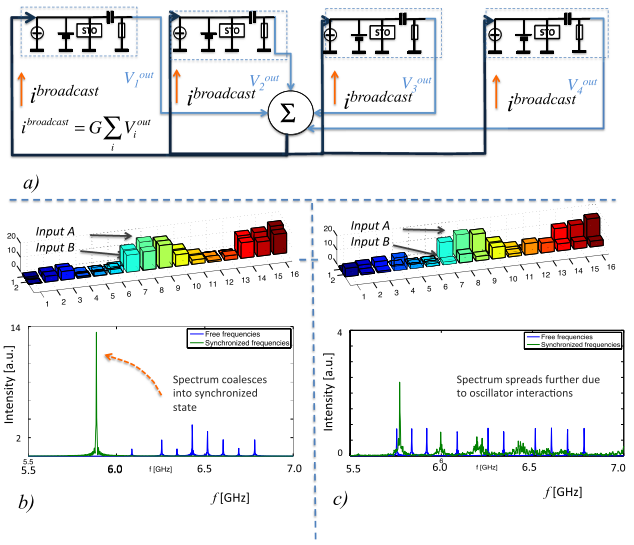

FIGURE 12. (a) Schematics of an electrically interconnected STO array, which is proposed for pattern matching applications. For simplicity, only four STOs are shown. Each STO is biased with the element-wise difference of two current vectors. The oscillatory output signal of the STOs is summed up, amplified and the resulting $i^{broadcast}$ signal is fed back to modulate all the STOs. The STO array behavior is shown (b) when inputs are matching vectors and when the difference between the vectors is large. In (b), all 16 STOs form a synchronized state, they all oscillate at the same frequency and with a narrow linewidth as seen on the STO spectra. In the nonmatched case, (c) each STO oscillates independently and with a large linewidth. Based on [22].

The I current vector is subsequently added to the bias currents of a network of identical, interconnected STOs, as shown in the circuit diagram of Fig. 12(a). The I currents change the free-running operating point of each STO. If the elements of I are small, then all the STO frequencies remain close together, and all the STOs will phase lock at a common frequency—this is exemplified in the simulation of Fig. 12(b). However, if pattern A and pattern B are sufficiently different (I has large values), then the resulting STO frequencies are shifted too far apart to collectively synchronize, as shown in Fig. 12(c). The presence or absence of collective synchronization is detectable on the STO oscillation spectra. Therefore, a measurement of this frequency distribution gives the length of I, which is a measure of the distance between the two images.

The frequency distribution can be straightforwardly detected by summing, rectifying, and integrating the oscillatory signals from the STOs. If the oscillators are synchronized to each other (and only in that case), then their oscillations are added coherently (in-phase), resulting in a large signal.

Detecting the distance between two analog patterns is a simple and fundamental operation in pattern recognition algorithms, but it is costly to implement in the traditional (analog or digital) CMOS circuitry. STOs may provide a more efficient realization, if this frequency distribution can

be efficiently detected, such as by a sum and filter operation or other analog measurements.

Another proposal for using oscillators as the components of associative memories uses modulating signals to interconnect oscillators that have distinct frequencies [25]. An f_0-frequency oscillator modulated with an f_m frequency signal develops sideband frequencies at $f_0 \pm f_m$ frequencies, and these sidebands may interact (synchronize) with other oscillators in the network. This scheme can realize all-to-all interconnections between the oscillators and can implement a Hopfield network [25]. Such an oscillatory Hopfield network [25] was recently demonstrated experimentally using electrical oscillators [21]. Here, use our circuit model for a proof of principle study that STOs may also be used as building blocks in oscillatory Hopfield networks.

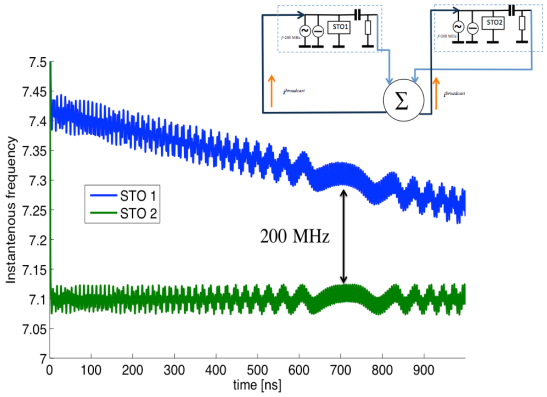

FIGURE 13. Plot of instantaneous frequency versus time, showing sideband synchronization via an ac coupling. An oscillatory modulation signal can connect and phase locking two STOs with very different frequencies. The instantenous frequencies are calculated from the time period of the oscillation, resulting in a noisy curve. The frequency of STO1 is locked to the sideband of STO1.

We study two electrically coupled STOs (STO1 and STO2), which were both modulated by a 200-MHz signal. This ac modulating current is superposed on the dc driving current of each STO. The interconnection scheme is shown in Fig. 13 (inset). In the simulation of Fig. 13, we slowly swept the current on STO1, changing its operating frequency. The previous simulations showed that the oscillators would not interact and phase lock until their frequencies are less than 50 MHz apart, due to the degree of coupling chosen. However, as shown in Fig. 13, when the mean oscillator frequency difference gets close to 200 MHz (the modulation frequency), the STO frequencies clearly became entrained. When the frequency of STO1 is swept further—closer to the mean frequency of STO2 but farther from the sideband—then the STOs again decouple. This indicates that the synchronization occurs via the sidebands.

These results indicate that STOs with significant frequency differences can be brought into interaction via externally applied oscillatory signals. This could become especially useful for practical reasons, since STOs often show large manufacturing variations, but using the scheme of [27], they still may serve as the components of oscillatory neural networks. In addition, this circuit architecture may enable the implementation of computational schemes that require dynamic or variable coupling strengths between oscillators [25].

IX. CONCLUSION

Nanocontact STOs show promise as fundamental elements for building arrays of phase-coherent oscillators for information processing and retrieval. STOs exhibit nonlinearities in current, field and spin waves that may be exploited in different ways to couple oscillators together. This paper reviewed recent results on the physics of stand-alone and interacting STOs and discussed methods for coupling STOs. These coupled STOs may serve as the basis of computing devices.

We have shown the experimental data for spin-wave-coupled and magnetic field-coupled STOs. Injection locking was also studied, which opens the way for electrical interconnection schemes. We described a simple circuit model of STOs that reproduces well the experimentally observed behaviors. Using this circuit model, elementary computing units were simulated. These units may serve as building blocks of complex image processing pipeline—additional components of the pipeline are introduced in [2].

For arrays of STOs to become functional circuit elements, several challenges must be overcome. First, the detailed compact models of the various coupling mechanisms must be formulated. This is hampered by the fact that while the basic physics of spin-transfer torques is reasonably well understood, many major features of the excitations themselves are not known, such as the excited mode's form, and its coupling to the surrounding magnetic environment. Once the coupling is better understood, scalable methods of modulating the interdevice coupling need to be found. In addition, many architectures that use arrays of oscillators require knowledge of the oscillator phase, and so require efficient, ideally nanoscale, methods of phase readout. Finally, the impact of device structure, including variations in fabrication and materials, on the device behavior must be understood, and controlled, to produce large arrays of oscillators with small deviations in frequency, linewidth, and power.

A central message of this paper is that STOs can be viewed as circuit blocks, and by interconnecting these circuit blocks one can design complex systems of synchronizing oscillators. These systems use frequency (or possibly phase) to represent information and may open new avenues in information processing that cannot be implemented in Boolean architectures.

Subsequent papers in this special section will describe how STO models can be used for the design and simulation of hierarchical systems, where STO arrays act as associative clusters and the associative clusters themselves serve as components of an image processing pipeline.

REFERENCES

[1] D. E. Nikonov *et al.* (2013). "Coupled-oscillator associative memory array operation." [Online]. Available: http://arXiv:1304.6125

[2] S. P. Levitan, Y. Fang, D. H. Dash, T. Shibata, D. E. Nikonov, and G. I. Bourianoff, "Non-Boolean associative architectures based on nano-oscillators," in *Proc. 13th Int. Workshop Cellular Nanosc. Netw. Appl.*, Aug. 2012, pp. 1–6.

[3] J. C. Slonczewski, "Current-driven excitation of magnetic multilayers," *J. Magn. Magn. Mater.*, vol. 159, nos. 1–2, pp. L1–L7, Jun. 1996.

[4] L. Berger, "Emission of spin waves by a magnetic multilayer traversed by a current," *Phys. Rev. B*, vol. 54, no. 13, p. 9353, 1996.

[5] G. Bertotti, C. Serpico, I. D. Mayergoyz, A. Magni, M. d'Aquino, and R. Bonin, "Magnetization switching and microwave oscillations in nanomagnets driven by spin-polarized currents," *Phys. Rev. Lett.*, vol. 94, no. 12, pp. 127206-1–127206-4, Apr. 2005.

[6] A. Slavin and V. Tiberkevich, "Nonlinear auto-oscillator theory of microwave generation by spin-polarized current," *IEEE Trans. Magn.*, vol. 45, no. 4, pp. 1875–1918, Apr. 2009.

[7] S. E. Russek, W. H. Rippard, T. Cecil, and R. Heindl, "Spin-transfer nano-oscillators," in *Handbook of Nanophysics: Functional Nanomaterials*. New York, NY, USA: CRC Press, 2010, pp. 1–24.

[8] W. H. Rippard, M. R. Pufall, S. Kaka, S. E. Russek, and T. J. Silva, "Direct-current induced dynamics in $Co_{90}Fe_{10}/Ni_{80}Fe_{20}$ point contacts," *Phys. Rev. Lett.*, vol. 92, no. 2, p. 027201, Jan. 2004.

[9] M. R. Pufall, W. H. Rippard, S. E. Russek, and E. R. Evarts, "Anisotropic frequency response of spin-torque oscillators with applied field polarity and direction," *Phys. Rev. B*, vol. 86, no. 9, pp. 094404–094410, Sep. 2012.

[10] M. W. Keller, M. R. Pufall, W. H. Rippard, and T. J. Silva, "Nonwhite frequency noise in spin torque oscillators and its effect on spectral linewidth," *Phys. Rev. B*, vol. 82, no. 5, p. 054416, Aug. 2010.

[11] W. H. Rippard, M. R. Pufall, S. Kaka, T. J. Silva, S. E. Russek, and J. A. Katine, "Injection locking and phase control of spin transfer nano-oscillators," *Phys. Rev. Lett.*, vol. 95, no. 6, p. 067203, Aug. 2005.

[12] S. Urazhdin, P. Tabor, V. Tiberkevich, and A. Slavin, "Fractional synchronization of spin-torque nano-oscillators," *Phys. Rev. Lett.*, vol. 105, no. 10, pp. 104101-1–104101-4, Aug. 2010.

[13] M. R. Pufall, W. H. Rippard, S. Kaka, T. J. Silva, and S. E. Russek, "Frequency modulation of spin-transfer oscillators," *Appl. Phys. Lett.*, vol. 86, no. 8, p. 082506, 2005.

[14] W. H. Rippard, M. R. Pufall, and A. Kos, "Time required to injection-lock spin torque nanoscale oscillators," *Appl. Phys. Lett.*, vol. 103, no. 18, p. 182403, 2013.

[15] S. Kaka, M. R. Pufall, W. H. Rippard, T. J. Silva, S. E. Russek, and J. A. Katine, "Mutual phase-locking of microwave spin torque nano-oscillators," *Nature*, vol. 437, no. 7057, pp. 389–392, Sep. 2005.

[16] F. B. Mancoff, N. D. Rizzo, B. N. Engel, and S. Tehrani, "Phase-locking in double-point-contact spin-transfer devices," *Nature*, vol. 437, no. 7057, pp. 393–395, Jul. 2005.

[17] M. R. Pufall, W. H. Rippard, S. E. Russek, S. Kaka, and J. A. Katine, "Electrical measurement of spin-wave interactions of proximate spin transfer nanooscillators," *Phys. Rev. Lett.*, vol. 97, no. 8, pp. 087206-1–087206-4, Aug. 2006.

[18] A. Ruotolo *et al.*, "Phase-locking of magnetic vortices mediated by antivortices," *Nature Nanotechnol.*, vol. 4, no. 8, pp. 528–532, Aug. 2009.

[19] W. H. Rippard *et al.*, "Spin-transfer dynamics in spin valves with out-of-plane magnetized CoNi free layers," *Phys. Rev. B*, vol. 81, p. 014426, Jan. 2010.

[20] M. J. Donahue and D. G. Porter. (Sep. 1999). OOMMF user's guide, version 1.0 interagency report NISTIR 6376. National Institute of Standards and Technology, Gaithersburg, MD, USA. [Online]. Available: http://math.nist.gov/oommf/

[21] X. Chen and R. H. Victora, "Phase locking of spin-torque oscillators by spin-wave interactions," *Phys. Rev. B*, vol. 79, p. 180402(R), May 2009.

[22] G. Csaba and W. Porod, "Computational study of spin-torque oscillator interactions for non-Boolean computing applications," *IEEE Trans. Magn.*, vol. 49, no. 7, pp. 4447–4451, Jul. 2013.

[23] M. Madami *et al.*, "Direct observation of a propagating spin wave induced by spin-transfer torque," *Nature Nanotechnol.*, vol. 6, pp. 635–638, Aug. 2011.

[24] H. Jaeger, W. Maass, and J. Principe, "Editorial: Special issue on echo state networks and liquid state machines," *Neural Netw.*, vol. 20, no. 3, pp. 287–289, 2007.

[25] F. C. Hoppensteadt and E. M. Izhikevich, "Oscillatory neurocomputers with dynamic connectivity," *Phys. Rev. Lett.*, vol. 82, pp. 2983–2986, Apr. 1999.

[26] F. Macià, A. D. Kent, and F. C. Hoppensteadt, "Spin-wave interference patterns created by spin-torque nano-oscillators for memory and computation," *Nanotechnology*, vol. 22, no. 9, p. 095301, 2011.

[27] R. W. Hölzel and K. Krischer, "Pattern recognition with simple oscillating circuits," *New J. Phys.*, vol. 13, p. 073031, Jul. 2011.

MATTHEW R. PUFALL, photograph and biography not available at the time of publication.

WILLIAM H. RIPPARD, photograph and biography not available at the time of publication.

GYÖRGY CSABA, photograph and biography not available at the time of publication.

DMITRI E. NIKONOV, photograph and biography not available at the time of publication.

GEORGE I. BOURIANOFF, photograph and biography not available at the time of publication.

WOLFGANG POROD, photograph and biography not available at the time of publication.